Effects of interface oxygen vacancies on electronic bands of FeSe/$SrTiO_3$(001)

M. X. Chen, Zhuozhi Ge, Y. Y. Li, D. F. Agterberg, L. Li, and M. Weinert
Department of Physics, University of Wisconsin–Milwaukee, Milwaukee, Wisconsin 53201
(Received 25 August 2016; revised manuscript received 12 December 2016; published 27 December 2016)

Modifications of the electronic bands of thin FeSe films due to oxygen vacancies in the supporting $SrTiO_3$(001) substrate—and the interplay with spin-orbit coupling, magnetism, and epitaxy—are investigated by first-principles supercell calculations. Unfolded (k-projected) bands show that the oxygen vacancies both provide electron doping to the interface FeSe layer and also have notable effects on the details of the bands around the Fermi level, including renormalizing the width of the Fe-3d band near the Fermi level by a factor of about 0.6 and causing a splitting of ∼40 meV at the M point for the checkerboard antiferromagnetic configuration. For an FeSe bilayer, the modifications to the bands are mainly limited to the interface FeSe layer. While spin-orbit-coupling induced band splittings of ∼30 meV at M for the ideal FeSe/$SrTiO_3$(001) interfaces are comparable to the splitting due to oxygen vacancies, the effects are not simply additive. Calculations and comparison to our scanning tunneling microscopy images of MBE-grown FeSe films on $SrTiO_3$(001) suggest that a common defect may be Se bound to an oxygen vacancy at the interface.

DOI: 10.1103/PhysRevB.94.245139

I. INTRODUCTION

Recently, the discovery of high T_c superconductivity in FeSe monolayers grown on $SrTiO_3$(001) (STO) has inspired intense interest in the FeSe/STO interface and FeSe thin films [1–6]. By means of *in situ* scanning tunneling microscopy (STM) Wang *et al.* observed a superconducting gap of about 20 meV for epitaxially grown FeSe monolayers after proper annealing, suggesting that the superconducting T_c in the grown FeSe monolayers may be as high as 77 K [1]. Subsequent transport measurements and angle-resolved photoemission spectroscopy (ARPES) experiments also observed high-T_c superconductivity in this system [7–13]. One puzzling feature of these observations is that the Fermi surface of the superconducting monolayer FeSe/$SrTiO_3$ is characterized by an electronlike pocket centered around the M points, while no pocket appears near the Γ point [10–13]. This challenges the Fermi surface nesting scenario that relies on nesting between M and Γ-point electronic states [14,15].

Although the mechanism of the high T_c superconductivity in the FeSe monolayers is under debate, there is consensus that the substrate plays an important role. For example, the induced strain on the FeSe films modifies the electronic properties [16]. In addition, it has been argued that the coupling of ferroelectric phonons in the substrate to electrons in FeSe may enhance the superconductivity [17]. Most importantly, the electronic properties of the grown FeSe monolayers are strongly dependent on annealing, i.e., the semiconducting as-grown FeSe monolayer becomes metallic upon proper annealing and then superconducting with further annealing [18]. However, FeSe multilayers show distinct differences in that they remain nonsuperconducting even after the annealing. This suggests that oxygen vacancies formed during annealing play an important role in the evolution of the electronic properties.

There have been a number of first-principles studies of both free-standing and supported FeSe thin films [19–28], investigating the effect of the $SrTiO_3$ substrate [20–24], surface adatoms [24,25], Se vacancies [26], electron doping [27,28], and oxygen vacancies (O-vac) [21–24]. It is found that there is no strong chemical bonding between the FeSe monolayer and perfect $SrTiO_3$(001), although the Se atoms in the FeSe monolayer do prefer the top sites of the cation atoms of the substrate [20]. The binding is enhanced by interface oxygen vacancies, which dope electrons into the FeSe monolayer, consequently modifying the Fermi surface of the overlayer [21–23]. The effect of oxygen vacancies on the bands of the nonmagnetic state has been investigated within the virtual crystal approximation, showing that the hole pockets around Γ are not fully removed [24]. However, thus far, the understanding of the effects of O vacancy at the interface between FeSe thin films and the SrTiO3(001) substrate remains incomplete, including issues related to the effect of oxygen vacancies on the electronic structures of FeSe layers both at the interface and farther away.

In this paper, we investigate the effects of interface O-vac on the electronic bands of FeSe monolayers and bilayers supported on $SrTiO_3$(001) by carrying out first-principles calculations. The O-vacant systems are modeled by supercells, and the unfolded bands are then obtained by projecting the supercell wave functions onto the 1×1 unit cell. It is found that the interfacial oxygen vacancy not only provides electron doping to the interface FeSe layer, but also has notable effects on the band details. In particular, for the checkerboard (CB) antiferromagnetic (AFM) state, the oxygen vacancies induce a band splitting at the M point (and along X-M), and lowers the Fe-3d_{z^2} states at the Γ point, thus significantly renormalizing the width of the Fe-3d band near the Fermi level. However, the effects of the O vacancy on the electronic properties of the top layer of bilayer FeSe are limited. In addition, spin-orbit coupling (SOC) can induce splittings at M comparable to those due to oxygen vacancies, demonstrating the possible importance of SOC in understanding this class of materials [29].

II. STRUCTURAL MODEL AND COMPUTATIONAL DETAILS

As shown in Fig. 1, the $SrTiO_3$(001) substrate (with a lattice constant of 3.905 Å) was modeled by a TiO_2-terminated slab consisting of five TiO_2 layers and four SrO layers, based on

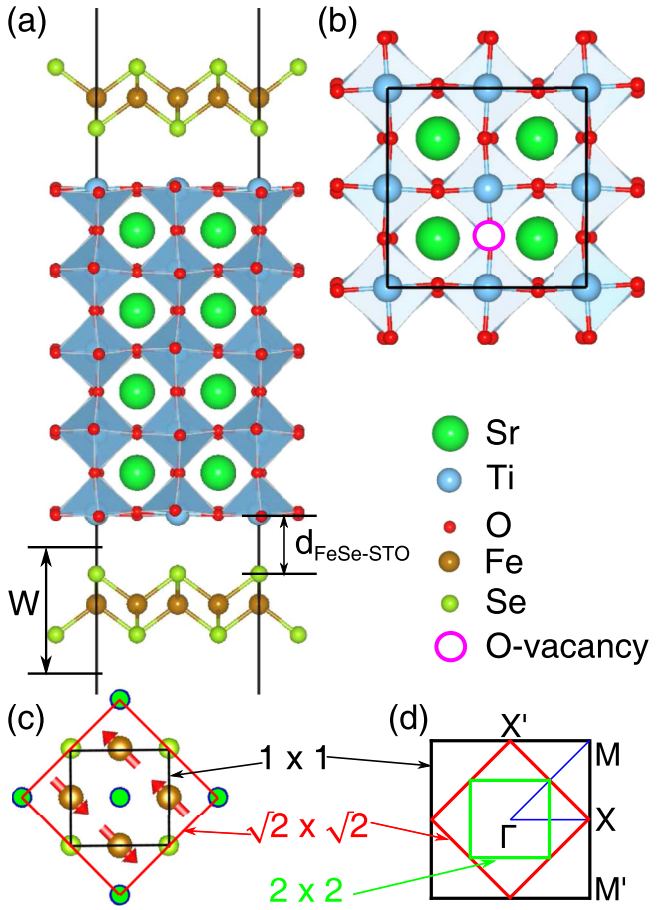

FIG. 1. Structural model of $FeSe/SrTiO_3(001)$. (a) Side view of monolayer $FeSe/SrTiO_3(001)$ in a 2×2 supercell. $d_{\text{FeSe-STO}}$ is the planar distance between the interface Ti and Se atoms. (b) Top view of 2×2 $SrTiO_3(001)$ with one O-vac. W represents the spatial window in which supercell wave functions are projected onto the (1×1) FeSe crystallographic (two Fe) cell. (c) Magnetic unit cell for CL-AFM denoted by the red box, which is in a $\sqrt{2} \times \sqrt{2}$ supercell. The crystallographic unit cell is represented by the black box. (d) Brillouin zones (BZs) of FeSe in the 1×1 unit cell, $\sqrt{2} \times \sqrt{2}$ and 2×2 supercells.

the relaxed structure of the antiferrodistortive $SrTiO_3$ bulk. To avoid dipole interactions between slabs, a single layer of FeSe is symmetrically placed on each side of $SrTiO_3(001)$. Two epitaxial relationships for the $FeSe/SrTiO_3(001)$ interface were considered: The bottom Se atoms sit directly above (i) the surface Ti atoms (type A), which was previously found to be more favorable compared to other configurations [20], or (ii) the surface O atoms (type B). Although the ideal type B interface is not energetically favorable, if there is a strong enough interaction between the oxygen vacancy and the Se, it is at least plausible that this epitaxial relationship could be nucleated; this issue is addressed below. The various $FeSe/SrTiO_3(001)$ slabs are separated from their periodic images by $\sim$20 Å vacuum regions. An oxygen vacancy is modeled by removing one surface oxygen atom in a 2×2 (or $\sqrt{2} \times \sqrt{2}$) supercell [STO-vac; see Fig. 1(b)]. The calculations were performed using the Vienna *ab initio* simulation package [30,31]. The exchange correlation functional is approximated by the generalized

TABLE I. Structural properties of the $FeSe/SrTiO_3(001)$ type A interfaces, both ideal and with an O vacancy, for different magnetic configurations. E_{tot} (in eV per FeSe unit cell) is the energy difference between magnetic states and the nonmagnetic state. $d_{\text{FeSe-STO}}$ (see Fig. 1) and $d_{\text{Fe-Se}}$ (in Å) are the interlayer distance and Fe-Se bond length, respectively; μ is the magnitude of the Fe magnetic moments.

	ideal			STO-vac		
	NM	CB-AFM	CL-AFM	NM	CB-AFM	CL-AFM
E_{tot}	0.00	−0.40	−0.55	0.00	−0.43	−0.51
$d_{\text{FeSe-STO}}$	3.00	2.98	3.00	2.82	2.80	2.82
$d_{\text{Fe-Se}}$	2.34	2.40	2.41	2.34	2.40	2.41
μ (μ_B)		2.11	2.40		2.04–2.15	2.34–2.45

gradient approximation as parametrized by Perdew, Burke, and Ernzerhof [32], and the pseudopotentials were constructed by the projector augmented wave method [33,34]. van der Waals (vdW) dispersion forces between the adsorbate and the substrate were included using the vdW-DF method developed by Klimeš and Michaelides [35]. An 8×8 Monkhorst-Pack k mesh was used to sample the surface BZ, and a plane-wave energy cutoff of 400 eV was used for structural relaxation and electronic structure calculations. For the structural relaxation only the FeSe and the top TiO_2 and SrO layers were allowed to relax, with a threshold of 0.001 eV/Å for the residual force on each atom while other atoms were held fixed. Three different magnetic configurations of the FeSe films were considered: nonmagnetic (NM), checkerboard antiferromagnetic (CB-AFM), and collinear antiferromagnetic (CL-AFM); the unstable ferromagnetic state is not considered. As shown in Table I, the CL-AFM configuration is calculated to be lower in energy than the CB-AFM, with the difference decreasing in the presence of oxygen vacancies. Although the FeSe may not have long-range magnetic order, these ordered calculations do provide insight into the effect of short-range magnetic order, which can have significant effects on the bands, i.e., nonmagnetic calculations are not good representations of paramagnetic systems if there are local moments. For the Fe-chalcogenides materials, even in the paramagnetic state, the NM calculated bands have Fermi surfaces and dispersions in disagreement with experiments [29]; we include the NM results here for comparison purposes even though these are not expected to correspond to the physical system.

The calculated electronic bands of the supported FeSe thin films used supercells, leading to band folding. To discern the effects of the interface O vacancy on the electronic bands of the FeSe overlayer (or different magnetic orderings), the supercell wave functions in FeSe (spatial window W shown in Fig. 1) were projected onto the corresponding k of the (1×1) FeSe cell using the layer k-projection technique [36–39]. This technique also allows for a more direct comparison to the photoemission results.

III. RESULTS AND DISCUSSION

A. Se-Ti (type A) interface

Table I summarizes the calculated structural properties of the interfaces of an FeSe monolayer with the ideal $SrTiO_3(001)$

substrate and with STO-vac. The interlayer distance $d_{\text{FeSe-STO}}$ remains almost unchanged for all the considered magnetic states. (The surface oxygen atoms are ∼0.08 Å above the Ti atoms.) The value of 2.98 Å for CB-AFM is slightly smaller than the 3.06 Å reported previously [20,27] as a result of the vdW correction, while the 3.0 Å for the CL-AFM state is consistent with Shanavas and Singh's calculation [24]. The Fe-Se bond lengths for the NM state are slightly shorter than those for the magnetic states. Although the two Se atoms are inequivalent because of the presence of the substrate, there is negligible difference in $d_{\text{Fe-Se}}$ for the two Se layers, implying that symmetry breaking in the supported FeSe monolayer due to the substrate is rather weak. Introduction of an O vacancy affects $d_{\text{FeSe-STO}}$ significantly and reduces the interlayer separation $d_{\text{FeSe-STO}}$ by about 10%, in agreement with a previous study [23]. However, the effect on the internal structure of the FeSe overlayer is negligible: $d_{\text{Fe-Se}}$ remains almost unchanged and the Fe atoms are still nearly co-planar. The induced variations of the Fe magnetic moments are in the range of 0.04–0.07 μ_B.

Figure 2 shows k-projected bands for supported FeSe in the different magnetic states, both with and without the interface O vacancy. Bands of the isolated FeSe monolayers with the same structure as in the supported case (i.e., with the substrate removed) are overlaid for comparison. Without the interface oxygen vacancy, Figs. 2(a)–2(c), the bands of the supported FeSe are similar to those of the free-standing FeSe monolayer. For the NM state, there are two hole bands near Γ and two electron bands around M crossing the Fermi level (E_F). For the CB-AFM state there is a hole band with a top that is slightly higher than E_F at Γ and a electron band around M, which is spin degenerate. The bands at Γ near E_F due to Fe-3d orbitals are pushed below E_F if a Hubbard-U correction is added [27]. For the CL-AFM state, there are hole bands crossing E_F near both Γ and M, in agreement with a previous study [20]. Figures 2(a)–2(c) also indicate that the ideal substrate has minor effects on the bands of FeSe near the Fermi level and a negligible shift of the Fermi level. For the NM state, the FeSe bands remain almost unaffected, except for a small shift of the states about Γ near −0.2 eV and the states about M near −0.4 eV. For the CB-AFM state, bands at Γ near −0.3 eV are shifted upward by about 0.1 eV.

Figures 2(d)–2(f) indicate that there is a significant shift of the Fermi level as a result of electron doping provided by the O vacancy. Accordingly, the electron pockets near Γ become smaller and the hole pocket about M becomes larger for the NM state. However, the main profile of FeSe bands is basically maintained, except for the bands about Γ at about −0.3 eV composed of Fe-3d_{xz,z^2}, which are shifted downward to −0.45 eV. For the CB-AFM state the O vacancy not only shifts E_F but also lowers the band at Γ. As a result, the hole pocket at Γ disappears and the bandwidth is renormalized by a factor of about 0.6. Moreover, it lifts the spin degeneracy of bands in between −0.3 eV and −0.2 eV along Γ-X-M, inducing a band splitting of about 40 meV at the M point. For the CL-AFM state, the pockets near Γ and near M are holelike. The empty states of FeSe are strongly perturbed by the hybridization with the substrate.

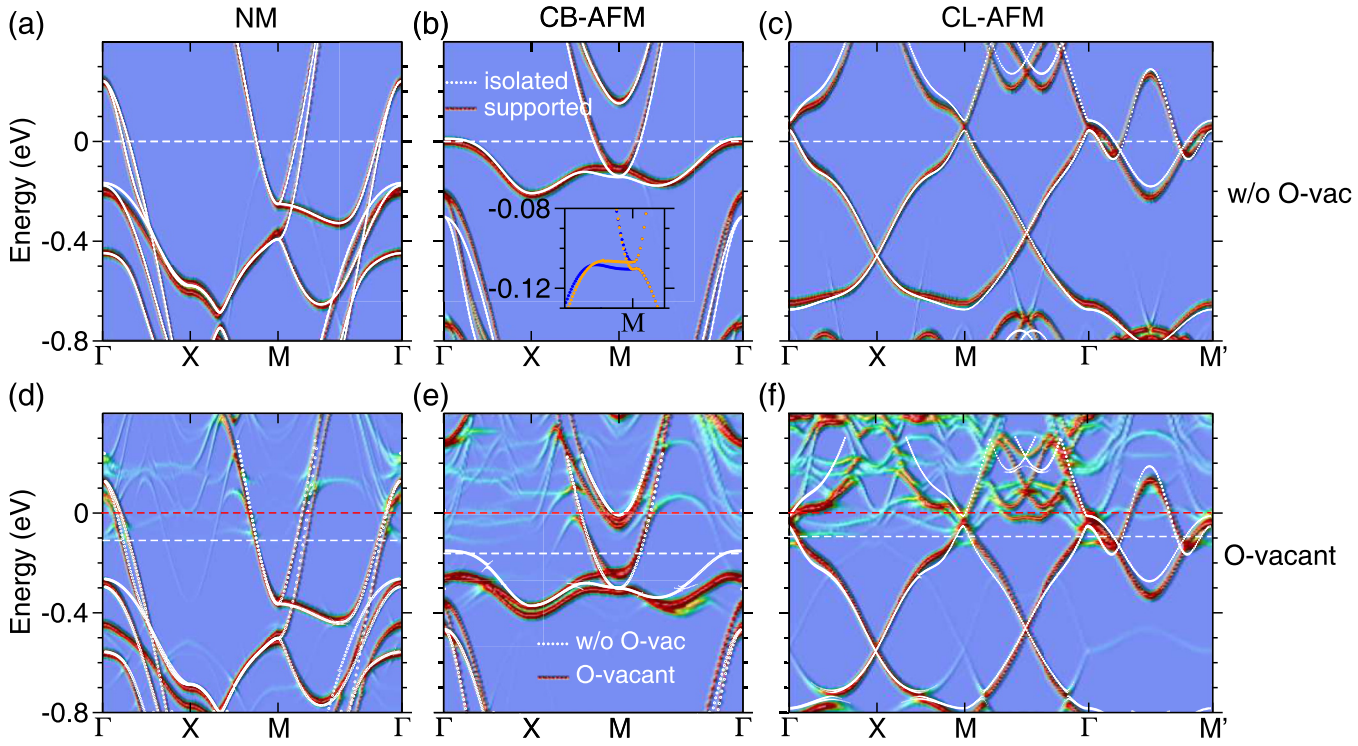

FIG. 2. k-projected bands for FeSe monolayers on $SrTiO_3$(001). Ideal interface for (a) NM, (b) CB-AFM (inset: expanded scale spin-resolved bands around M), and (c) CL-AFM magnetic configurations. (d)–(f) Corresponding bands for oxygen vacancy. Bands for isolated FeSe layers with the same internal (relaxed) structure (white) are overlaid for comparison. White and red dashed lines denote the Fermi levels of the isolated and supported FeSe, respectively.

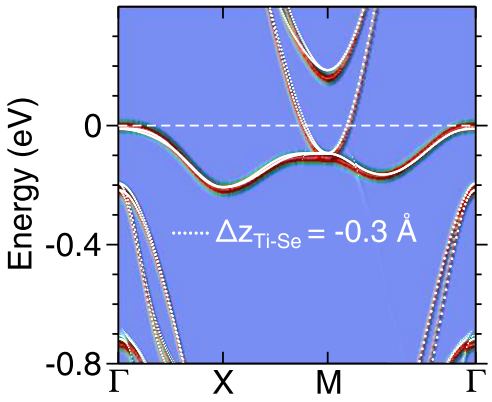

FIG. 3. Comparison of bands for the perfect FeSe/$SrTiO_3$(001) at the equilibrium interlayer distances and at a reduced (by 0.3 Å) interlayer separation.

The significant difference in the electronic bands for CB-AFM configuration with and without the O vacancy is related to the structural differences. Table I shows that the structure of FeSe thin films remains almost unaffected, but the interlayer distance is considerably reduced in the presence of the O vacancy, which may strengthen the interaction between the overlayer and the substrate, including inducing more charge transfer between them. To study the effect of the interlayer separation, calculations were done for ideal FeSe/$SrTiO_3$(001) with the interlayer distance reduced by 0.3 Å. Figure 3 indicates that the FeSe bands are basically unaffected. Therefore, the dramatic changes in the bands of FeSe can be attributed to the O vacancy, which both dopes electrons to the FeSe overlayer and pins the Fermi level of the FeSe to the substrate band gap. Indeed, previous calculations have demonstrated that bands at M and Γ for the freestanding CB-AFM FeSe are sensitive to charge doping [27].

The bands for an FeSe bilayer on $SrTiO_3$(001) with an oxygen vacancy are shown in Fig. 4. One important feature that can be seen from Fig. 4 is that the k-projected bands for the interface layer are similar to those for monolayer FeSe/STO-vac, while the bands for the top layer [Figs. 4(d)–4(f)] resemble those for the perfect FeSe/STO. In particular, a comparison of Figs. 4(b) and 4(e) indicates that for the CB-AFM state, the band splitting at M point is almost negligible for the top layer and a pocket appears at Γ. For the CL-AFM state, the strong band hybridization between empty states of the interface FeSe layer and the substrate along M-Γ [Fig. 4(c)] is not seen for the top layer. This indicates that the O vacancy has little effect on the top layer, which stems from the interface FeSe layer effectively screening the charges created by the interface O vacancy. This is consistent with previous calculations that find that charges induced by the O vacancy are mainly distributed at the interface [22].

B. Dependence on oxygen-vacancy concentration

Because the bands near Γ and M for the CB-AFM state are sensitive to oxygen vacancies, calculations were also performed for $2\sqrt{2} \times 2\sqrt{2}$ O-vacant FeSe/$SrTiO_3$(001) to see how the bands change as the concentration of O-vac varies. The substrate was modeled by a single $SrTiO_3$ layer for computational reasons. In this case, the concentration of O-vac is half of that for 2×2 O-vacant FeSe/$SrTiO_3$(001),

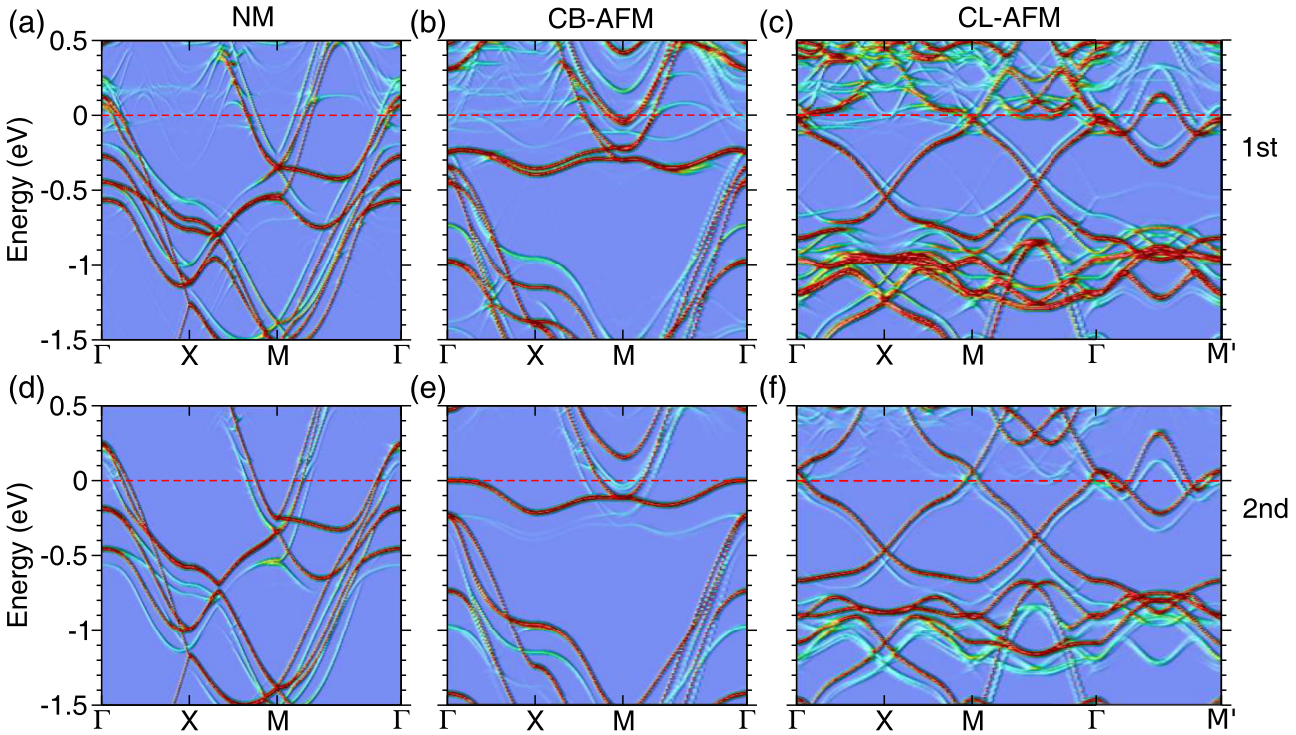

FIG. 4. k-projected bands for bilayer FeSe on $SrTiO_3$(001) with an O vacancy in different magnetic configurations for (a)–(c) the interface and (d)–(f) top FeSe layer in the NM, CB-AFM, and CL-AFM states, respectively.

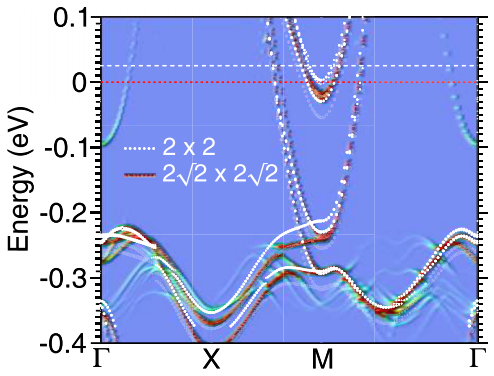

FIG. 5. k-projected bands for CB-AFM FeSe monolayers on $SrTiO_3$(001) with one O-vac in a $2\sqrt{2} \times 2\sqrt{2}$ supercell. The band structure for 2×2 O-vacant FeSe/$SrTiO_3$(001) (white curves, corresponding to the peaks of the k-projected FeSe bands in Fig. 2(e), i.e., removing bands with low weight) is overlaid for comparison. The red (white) dashed line represents the Fermi level of $2\sqrt{2} \times 2\sqrt{2}$ (2×2) O-vacant FeSe/$SrTiO_3$(001).

which gives rise to less charge transfer between FeSe and $SrTiO_3$(001). Figure 5 shows that the overall band structure changes slightly. The Fermi level shifts to a slightly lower energy (Fig. 5), consistent with a lower O-vac concentration. The gap at M located at about -0.25 eV decreases slightly with lower O-vac concentration.

C. Spin-orbit coupling

Spin-orbit coupling has been shown to affect the band structure in the Fe-based superconductors [29,40]. In particular, it lifts the degeneracy at the zone center, inducing a band splitting of ∼50 meV for $FeTe_{0.5}Se_{0.5}$ [29]. The effects of SOC on the bands of FeSe films on $SrTiO_3$, both with and without the interfacial O-vac, are summarized in Fig. 6. One can see that SOC has noticeable effects on the topology of electronic bands. It induces band splittings (green circles) at/near the M point where there is a band crossing in the non-SOC calculations. For the NM state SOC induces a splitting of about 60 meV for bands about 0.2 eV above the Fermi level at Γ for the perfect FeSe/$SrTiO_3$(001) [Fig. 6(a)] and reduces the gap at M. For the CB-AFM configuration, SOC enhances the gap at M near E_F by ∼30 meV [Fig. 6(b)]; similar splittings of about 30 meV are induced for the CL-AFM state.

The interfacial oxygen vacancy, which also caused band splittings, will modify these splittings. For the NM state, a comparison of Figs. 6(a) and 6(d) shows that the presence of the interfacial O-vac enhances the SOC-induced shift of the band near -0.3 eV at Γ by ∼30 meV. For the CL-AFM, the O-vac has little effects on SOC splittings, while for CB-AFM, Fig. 6(e), the gap at M is enhanced by only about 5 meV. Figure 7 further depicts the dependence of the SOC splitting on the O-vac concentration for the CB-AFM state and shows that the effects of SOC and the oxygen vacancies are not simply additive. This observation should not be surprising since even in perturbation theory starting from states that are already split (either by SOC or O vacancies), adding in the other effect will be suppressed because of the energy denominator. Note, however, that the SOC contribution will cause a splitting for all vacancy contributions, while the additional splitting attributable to the oxygen vacancies will scale (in a complicated manner) with the vacancy concentration. There is, however, a distinction between the SOC- and O vacancy-induced splittings mainly along X-M, and to a lesser extent along Γ-X.

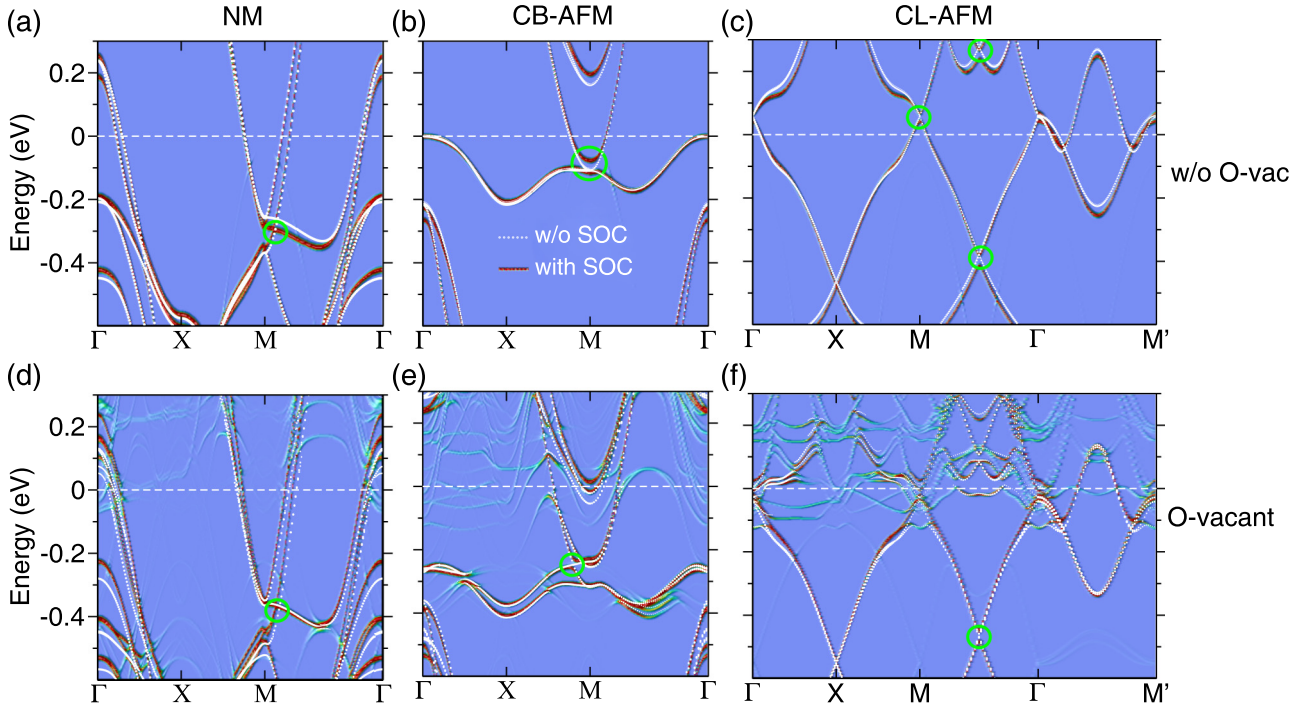

FIG. 6. k-projected bands with SOC for (a)–(c) ideal and (d)–(f) O-vacant FeSe/$SrTiO_3$(001). Bands without SOC (white curves) are overlaid for comparison. Green circles mark SOC-induced band splittings where bands are (nearly) degenerate without SOC.

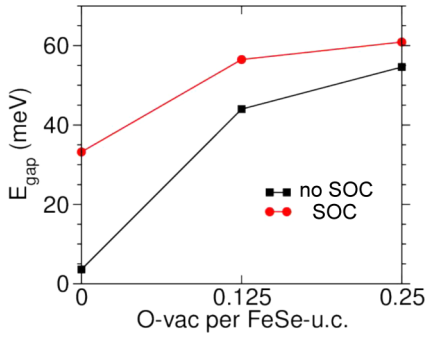

FIG. 7. Effect of O-vac concentration on the gap near the Fermi level at M for the CB-AFM state. 0.125 (0.25) O-vac/FeSe-u.c. corresponds to the $2\sqrt{2} \times 2\sqrt{2}$ (2 × 2) O-vacant FeSe/$SrTiO_3$(001).

D. Bands around Γ and M

Details of bands near Γ and M for FeSe thin films on $SrTiO_3$ were investigated by ARPES experiments [10–13,17]. It was observed that the Fermi surface of monolayer FeSe/$SrTiO_3$ consists of electronlike pockets at M with a band bottom 60 meV below the Fermi level [10–13]. Further analysis reveals that there are two nearly degenerate electron bands [17]. Moreover, there is one holelike band about 40 meV below the bottom of the electronlike band. At Γ there is one holelike band with a top located 80 meV below E_F. In the case of bilayer FeSe/$SrTiO_3$ there are several holelike bands right below E_F at Γ. There are four small pockets forming a cross-shaped Fermi surface centered around M. Detailed band structure reveals that they result from the crossing of a holelike band and an electronlike band. At the M point there is another holelike band below the Fermi level with a top at 60 meV below E_F which has a energy separation of about 80 meV from the higher hole band. The separation/splitting reduces dramatically as the k point goes further away from M (Fig. S2 in Ref. [12]).

Our calculations show that both the NM state and the CL-AFM state give rise to large pockets around Γ, inconsistent with the experimental observations. In contrast, for the CB-AFM state [Fig. 2(e)] there is no pocket near Γ and only electron pockets centered about M, consistent with the ARPES results. Since in the present study a 2 × 2 supercell with one O vacancy was used to model the substrate, this gives rise to a much higher doping level than experiment and results in a larger shift of the Fermi level. Based on these considerations, we rigidly shift down the Fermi level such that it corresponds to a lower doping level (∼0.2 e^-/Fe); based on the 2 × 2 and $\sqrt{2} \times \sqrt{2}$ supercells, a single oxygen vacancy dopes ∼1.6–1.7 electrons into the FeSe overlayer. Figs. 8(a) and 8(b) show bands about Γ and M, respectively. One can see that there are two nearly degenerate electron bands about M, where the band splitting between the electron band and the hole band is ∼40 meV, consistent with the ARPES experiments. In addition, the width of the bands of interest about Γ and M are also in agreement with ARPES results (Fig. 3 in Ref. [13]) without any rescaling. The shape of the top of the hole band at Γ as well as M is sensitive to lattice constant, which becomes round for smaller in-plane lattice constants. The replica bands seen by the ARPES experiments [17] do not appear in our calculations; these have been attributed to the coupling of FeSe bands to the substrate ferroelectric phonons.

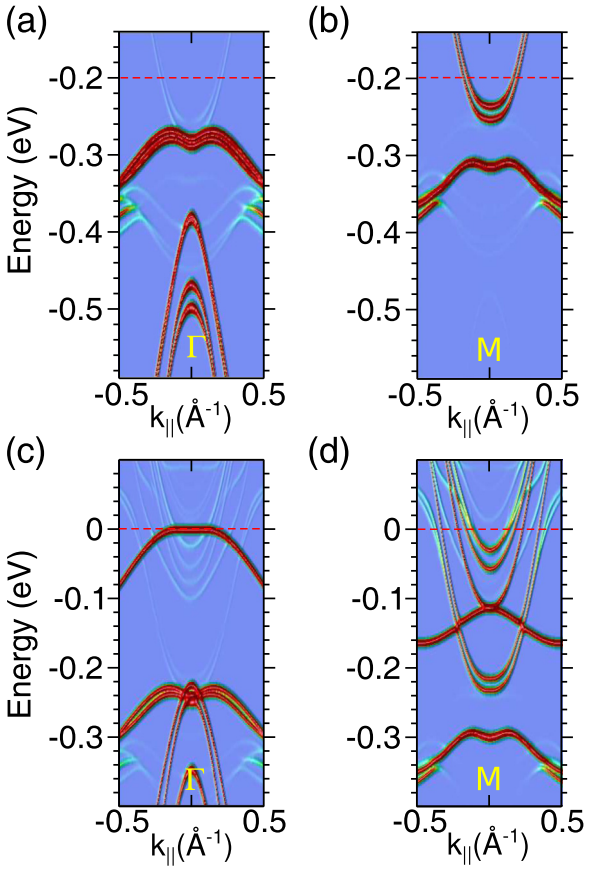

FIG. 8. Bands for FeSe monolayer on STO-vac (a) around Γ (along M-Γ-M) and (b) M (along Γ-M-Γ), and the (c) and (d) corresponding bands for an FeSe bilayer.

For bilayer FeSe/$SrTiO_3$(001), the Fermi level of the top FeSe layer stays nearly unchanged in the presence of the O vacancy. Figure 8(c) shows that there is only one holelike band at Γ near E_F, differing from the ARPES measurements which observe multiple hole bands. In Fig. 8(d), the splitting of about 180 meV between the two holelike bands at the M point is much larger than that is seen by the experiments, and the splitting tends to increase as the k moves away from M, in contrast to the experimental observations. Shifting the bands of the interface FeSe layer to account for a lower electron doping and then superimposing them onto those for the top FeSe layer does not improve the agreement. Given that the 80 meV splitting of the two hole bands at M are common for FeSe thin films thicker than monolayer [12], the discrepancy between our calculations and ARPES measurements is unclear, but might be attributed to nematicity in FeSe, which is not directly taken into account in our calculations.

E. Se-O (type B) interface

Up to now, we have focused on the Type A, Se-Ti, epitaxial relationship since this is preferred for the ideal interface. The overall energetics do not change in the presence of an oxygen vacancy: for example, our calculations for $2\sqrt{2} \times 2\sqrt{2}$

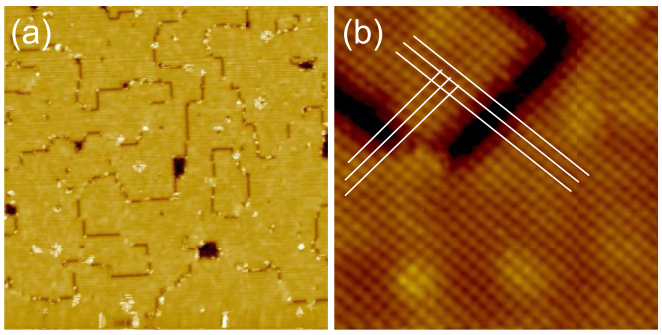

FIG. 9. (a) STM image of a MBE-grown FeSe monolayer film on $SrTiO_3(001)$ ($V_s = 1.5$ V, $I_t = 0.2$ nA, 100 nm $\times$ 100 nm). (b) Close-up view of a grain boundary ($V_s = -0.5$ V, $I_t = 1.5$ nA, 10 nm $\times$ 10 nm). The lines are guides to show the relative shift in alignment between the two grains.

O-vacancy FeSe/$SrTiO_3(001)$ supercells, Type A (Se-Ti) is 0.25 eV FeSe-u.c. lower than the Type B (Se-O), in large part because of the increase in the interlayer distance to about 3.34 Å. Despite these energetics, if the oxygen vacancy were to nucleate a type B registry of the FeSe film, the barrier to shift may be large enough to pin the film.

Experimentally, there is evidence for different possible epitaxial relationships. The growth of FeSe films was carried out in an integrated MBE-STM ultrahigh vacuum system with a base pressure of 2×10^{-11} Torr. Monolayer and bilayer FeSe films were grown on 0.05 wt% Nb-doped $SiTiO_3(001)$ substrates, which were first annealed at 900 °C in Se flux. Then the FeSe films were grown under Se-rich conditions with a growth rate of 0.2 monolayers per minute. Monolayer FeSe films were further annealed at ~500 °C for 2–3 hours to remove adsorbed Se and to reach a superconducting state with a paring gap of ~20 meV, consistent with the earlier studies [1]. Scanning tunneling microscopy (STM) images, Fig. 9, show that the films consist of large grains, with their crystallographic axes aligned, presumably with the $SrTiO_3$. However, as shown in the atomic resolution image in Fig. 9(b), the films across a grain boundary can be shifted relative to each, i.e., the FeSe films may have various epitaxial relationships to the $SrTiO_3$ substrate.

The unfolded bands for the CB-AFM type B interface (with O vacancy) is shown in Fig. 10(a). Comparing to Fig. 5 shows that there is only a small shift of the Fermi level, implying less charge transferred to the FeSe layer for this configuration, due in part to the increased separation. Artificially reducing the layer distance by about 0.8 Å, Fig. 10(b), leads to a strong hybridization between the FeSe monolayer and the substrate [Fig. 10(b)], causing noticeable changes around the M point.

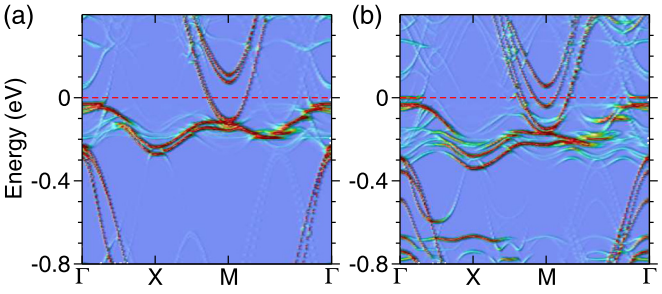

FIG. 10. Electronic bands for the CB-AFM FeSe in Type B registry (Se above O) for $2\sqrt{2} \times 2\sqrt{2}$ O-vacancy FeSe/$SrTiO_3(001)$ at (a) the equilibrium and (b) reduced (by 0.8 Å) interlayer separation.

F. Se-O vacancy binding

Although oxygen vacancies are expected surface defects of $SrTiO_3$, it is not obvious that these will be the dominant defects in the combined system since experimentally the surfaces of $SrTiO_3$ are treated by Se flux before the growth of FeSe thin films [1]. This raises the possibility that Se interacts with the oxygen vacancies. Our calculations show that a single Se has a strong tendency to bind to an O vacancy: A single Se on $SrTiO_3(001)$ with one O-vac in a $2\sqrt{2} \times 2\sqrt{2}$ supercell prefers the binding to the O vacancy rather than to a Ti by 1.20 eV, i.e., Se have a strong driving force to saturate O vacancies. The bond lengths of Se and its neighboring Ti atoms are about 2.52 Å. Introducing another Se originally sitting on the top site of the O near the O-vac leads to the formation of Se dimer of Se after structural relaxation [hereafter referred to as S1, Figs. 11(a), and 11(b)]. The Se binding to the O-vac moves further away from the $SrTiO_3(001)$ surface such that one Se-Ti bond is increased up to about 2.70 Å. The second Se is further away from the $SrTiO_3(001)$ surface by about 1.02 Å than the one sitting on the O-vac. Another configuration [S2, Figs. 11(c) and 11(d)] with the second Se originally placed on the top site of Ti near the O-vac is only 0.06 eV/Se higher than S1, indicating the tendency of Ti as the preferable sites for Se when the O-vac is saturated. Thus, if Se atoms can saturate the oxygen vacancies, then a type A interface may result.

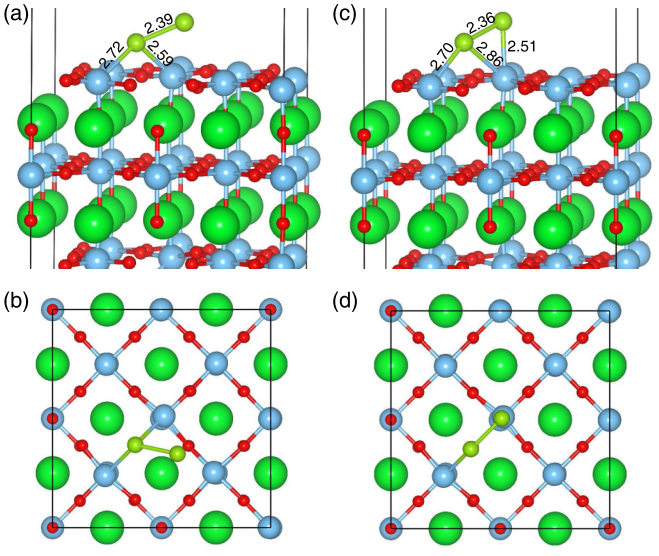

FIG. 11. Calculated structure of two Se deposited onto $SrTiO_3(001)$ with one O vacancy in a $2\sqrt{2} \times 2\sqrt{2}$ supercell. The two lowest-energy configurations out of the considered candidates are shown: (a) Perspective and (b) top views of configuration S1, obtained from the structural relaxation starting with the second Se sitting on an oxygen atom close to the O-vac; (c) and (d) same for S2. Bond lengths involving Se are shown (in Å).

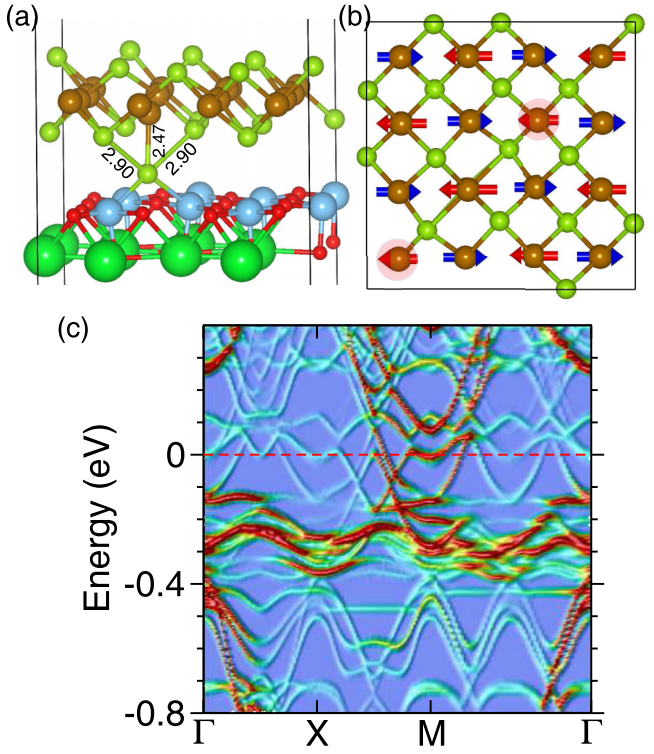

FIG. 12. Se-O vacancy Type A FeSe/$SrTiO_3$(001) interface: (a) Perspective view of the relaxed structure for CB-AFM $2\sqrt{2} \times 2\sqrt{2}$ cell, and (b) schematic of the magnetic structure (shaded atoms indicate that the moments on them are significantly reduced). (c) k-projected band structure.

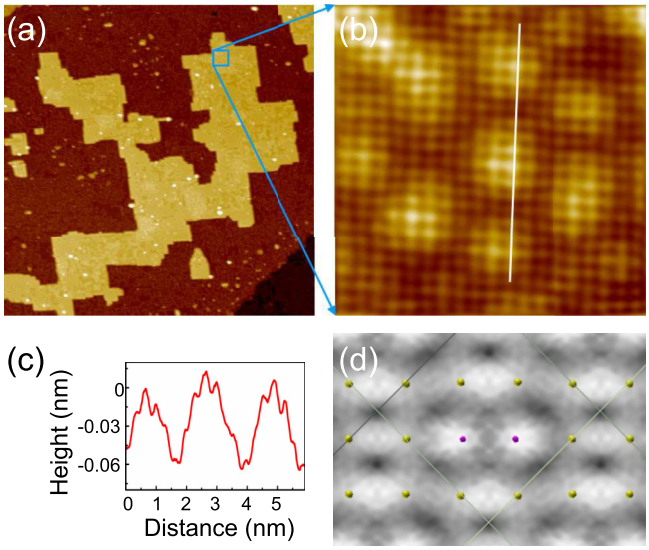

FIG. 13. (a) STM image showing monolayer FeSe islands on $SrTiO_3$(001) ($V_s = 1.0$ V, $I_t = 0.1$ nA, 200 nm × 200 nm). (b) Atomic resolution image of the boxed region in (a) ($V_s = 1.0$ V, $I_t = 0.1$ nA, 10 nm × 10 nm). (c) Line profile (height variations) along the line shown in (b). (d) Calculated STM image for an FeSe monolayer on the Se–O-vacancy complex. The positions of the uppermost Se atoms are indicated; the purple dots indicate the Se atoms closest to the defect, which are pulled down by ∼0.25 Å relative to the other Se atoms. (Constant current/density simulation: 1 V bias, $2 \times 10^{-8} e/Å^3$; nominal average height of 4.6 Å above the surface, with a corrugation of ±0.06 Å).

Because Se is isovalent to O, filling the O-vac by Se may be expected, which gives rise to similar geometric and electronic properties as the perfect FeSe/$SrTiO_3$(001). However, our calculations reveal that the filled Se induces dramatic changes in the structure of the FeSe monolayer. The calculation was carried out for the CB-AFM $2\sqrt{2} \times 2\sqrt{2}$ FeSe/$SrTiO_3$(001) where the two constituents are in Se-Ti (Type A) stacking. The relaxed structure is shown in Fig. 12(a). The extra Se forms direct bonding with the Fe sitting above it, which pulls the Fe out (down) of the Fe plane by about 0.55 Å. The two surface Se atoms binding to the downward-shifted Fe are correspondingly shifted, that is, they are pulled closer to the Fe plane by about 0.25 Å.

Defects in MBE-grown FeSe films are not unusual. A common defect appears as enhanced contrast over ∼4 unit cells, with a height fluctuation of several hundredths of a nm, c.f., Figs. 13(a) and 13(b) and is seen throughout the sample. Although direct comparisons between the experiments and calculations are not feasible because of much larger supercells required, our results are at least suggestive. In contrast to the oxygen vacancy case in which the interlayer separation between the FeSe and substrate decreases, for the Se–O-vacancy complex there is an increase of 0.1–0.2 Å. Although low compared to the values in Fig. 13(c) (and closer to the values calculated for the Type B interface), there is not a simple one-to-one relationship between the STM height differences and the atom positions. In fact, the simulated STM image, Fig. 13(d), shows enhanced corrugation at the Se atoms nearest the defect complex, despite the fact that these are 0.25 Å lower. We note that simulated STM images (not shown) for the simple O vacancy and the type B interface appear less consistent with the experimental data. While the present results do not conclusively demonstrate that Se–O-vacancy complexes exist, they do strongly suggest that defect complexes—not just simple oxygen vacancies—exist at the substrate-FeSe interface and can modify the electronic properties.

This conclusion is borne out in the calculations for FeSe at the Se–O-vacancy interface. There is no net magnetic moment for the ideal free-standing AFM FeSe monolayer, but in proximity to either the ideal or the O-vacant $SrTiO_3$(001), small (<0.06 μ_B) net magnetic moments are induced due to inversion-symmetry breaking. When the Se fills the O vacancy, changes in the Fe magnetic moments give rise to a net magnetic moment of about 1.0 μ_B for the FeSe overlayer. The moment on the downward-shifted Fe is significantly enhanced by about 0.5 μ_B, and a general increase in that spin channel, except for the two Fe atoms marked in Fig. 12(b), which are reduced by about 0.3 μ_B. The dramatic change in the magnetism has an important effect on the band structure of the FeSe monolayer. Figure 12(c) shows that the electronic bands of FeSe are strongly disturbed by the fluctuating magnetism, though the global profile is similar to that for CB-AFM FeSe monolayer. A comparison of Fig. 12(c) and Fig. 5 shows that the size of the electron pockets centered at M decreases, suggesting that the extra Se lowers the doping level of the FeSe overlayer. It should be noted that the origin of the doping to the FeSe monolayer

on Se-filled $SrTiO_3(001)$ is different from that for O-vacant $FeSe/SrTiO_3(001)$; in the former case, the doping is due to the charge transfer between the extra Se and the FeSe overlayer, whereas, in the latter the O-vac is mainly responsible for the doping.

IV. SUMMARY

In summary, we have investigated the effects of oxygen vacancies at the interface of between FeSe thin films and $SrTiO_3(001)$. The interface oxygen vacancy not only provides electron doping to the interface FeSe layer but also significantly renormalizes the width of the Fe-3*d* band near the Fermi level for the checkerboard AFM state. However, due to the screening of the interface FeSe layer, the effects of the O vacancy on the electronic properties of the top FeSe layer in bilayer FeSe are limited, e.g., the electronic bands for the top FeSe layer are similar to the perfect monolayer $FeSe/SrTiO_3(001)$. Spin orbit is also found to play an important role in determining the detailed band structure, giving rise to splittings both for the ideal case and in the presence of defects. Our results suggest that while different epitaxial relationships are possible in the presence of simple oxygen vacancies, a likely defect is a Se–O-vacancy, with then "standard" type A (Se-Ti) registry. The calculated bands around Γ and *M* for the checkerboard-AFM monolayer $FeSe/SrTiO_3(001)$ in the presence of oxygen vacancies are generally consistent with ARPES results. However, for the bilayer case the agreement is not particularly good, which requires further investigations. Finally, our results demonstrate that understanding the detailed electronic properties requires treating a number of different effects on an equal footing: short- and long-range magnetic correlations, spin-orbit, epitaxial relationships, and defect complexes.

ACKNOWLEDGMENT

This work was supported by the U.S. National Science Foundation, Division of Materials Research, DMR-1335215.

[1] W. Qing-Yan, L. Zhi, Z. Wen-Hao, Z. Zuo-Cheng, Z. Jin-Song, L. Wei, D. Hao, O. Yun-Bo, D. Peng, C. Kai, W. Jing, S. Can-Li, H. Ke, J. Jin-Feng, J. Shuai-Hua, W. Ya-Yu, W. Li-Li, C. Xi, M. Xu-Cun, and X. Qi-Kun, Chin. Phys. Lett. **29**, 037402 (2012).

[2] D. Huang, C.-L. Song, T. A. Webb, S. Fang, C.-Z. Chang, J. S. Moodera, E. Kaxiras, and J. E. Hoffman, Phys. Rev. Lett. **115**, 017002 (2015).

[3] G. Zhou, D. Zhang, C. Liu, C. Tang, X. Wang, Z. Li, C. Song, S. Ji, K. He, L. Wang, X. Ma, and Q.-K. Xue, Appl. Phys. Lett. **108**, 202603 (2016).

[4] P. Zhang, X.-L. Peng, T. Qian, P. Richard, X. Shi, J.-Z. Ma, B.-B. Fu, Y.-L. Guo, Z. Q. Han, S. C. Wang, L. L. Wang, Q.-K. Xue, J. P. Hu, Y.-J. Sun, and H. Ding, Phys. Rev. B **94**, 104510 (2016).

[5] Y. Miyata, K. Nakayama, K. Sugawara, T. Sato, and T. Takahashi, Nat. Mater. **14**, 775 (2015).

[6] J. Shiogai, Y. Ito, T. Mitsuhashi, T. Nojima, and A. Tsukazaki, Nat. Phys. **12**, 42 (2016).

[7] Z. Wen-Hao, S. Yi, Z. Jin-Song, L. Fang-Sen, G. Ming-Hua, Z. Yan-Fei, Z. Hui-Min, P. Jun-Ping, X. Ying, W. Hui-Chao, F. Takeshi, H. Akihiko, L. Zhi, D. Hao, T. Chen-Jia, W. Meng, W. Qing-Yan, H. Ke, J. Shuai-Hua, C. Xi, W. Jun-Feng, X. Zheng-Cai, L. Liang, W. Ya-Yu, W. Jian, W. Li-Li, C. Ming-Wei, X. Qi-Kun, and M. Xu-Cun, Chin. Phys. Lett. **31**, 017401 (2014).

[8] Y. Sun, W. Zhang, Y. Xing, F. Li, Y. Zhao, Z. Xia, L. Wang, X. Ma, Q.-K. Xue, and J. Wang, Sci. Rep. **4**, 6040 (2014).

[9] J.-F. Ge, Z.-L. Liu, C. Liu, C.-L. Gao, D. Qian, Q.-K. Xue, Y. Liu, and J.-F. Jia, Nat. Mater. **14**, 285 (2015).

[10] D. Liu, W. Zhang, D. Mou, J. He, Y.-B. Ou, Q.-Y. Wang, Z. Li, L. Wang, L. Zhao, S. He, Y. Peng, X. Liu, C. Chen, L. Yu, G. Liu, X. Dong, J. Zhang, C. Chen, Z. Xu, J. Hu, X. Chen, X. Ma, Q. Xue, and X. J. Zhou, Nat. Commun. **3**, 931 (2012).

[11] S. He, J. He, W. Zhang, L. Zhao, D. Liu, X. Liu, D. Mou, Y.-B. Ou, Q.-Y. Wang, Z. Li, L. Wang, Y. Peng, Y. Liu, C. Chen, L. Yu, G. Liu, X. Dong, J. Zhang, C. Chen, Z. Xu, X. Chen, X. Ma, Q. Xue, and X. J. Zhou, Nat. Mater. **12**, 605 (2013).

[12] S. Tan, Y. Zhang, M. Xia, Z. Ye, F. Chen, X. Xie, R. Peng, D. Xu, Q. Fan, H. Xu, J. Jiang, T. Zhang, X. Lai, T. Xiang, J. Hu, B. Xie, and D. Feng, Nat. Mater. **12**, 634 (2013).

[13] X. Liu, D. Liu, W. Zhang, J. He, L. Zhao, S. He, D. Mou, F. Li, C. Tang, Z. Li, L. Wang, Y. Peng, Y. Liu, C. Chen, L. Yu, G. Liu, X. Dong, J. Zhang, C. Chen, Z. Xu, X. Chen, X. Ma, Q. Xue, and X. J. Zhou, Nat. Commun. **5**, 5047 (2014).

[14] I. I. Mazin, D. J. Singh, M. D. Johannes, and M. H. Du, Phys. Rev. Lett. **101**, 057003 (2008).

[15] K. Kuroki, S. Onari, R. Arita, H. Usui, Y. Tanaka, H. Kontani, and H. Aoki, Phys. Rev. Lett. **101**, 087004 (2008).

[16] R. Peng, H. C. Xu, S. Y. Tan, H. Y. Cao, M. Xia, X. P. Shen, Z. C. Huang, C. H. P. Wen, Q. Song, T. Zhang, B. P. Xie, X. G. Gong, and D. L. Feng, Nat. Commun. **5**, 5044 (2014).

[17] J. J. Lee, F. T. Schmitt, R. G. Moore, S. Johnston, Y.-T. Cui, W. Li, M. Yi, Z. K. Liu, M. Hashimoto, Y. Zhang, D. H. Lu, T. P. Devereaux, D.-H. Lee, and Z.-X. Shen, Nature (London) **515**, 245 (2014).

[18] W. Zhang, Z. Li, F. Li, H. Zhang, J. Peng, C. Tang, Q. Wang, K. He, X. Chen, L. Wang, X. Ma, and Q.-K. Xue, Phys. Rev. B **89**, 060506 (2014).

[19] T. Bazhirov and M. L. Cohen, J. Phys.: Condens. Matter **25**, 105506 (2013).

[20] K. Liu, Z.-Y. Lu, and T. Xiang, Phys. Rev. B **85**, 235123 (2012).

[21] J. Bang, Z. Li, Y. Y. Sun, A. Samanta, Y. Y. Zhang, W. Zhang, L. Wang, X. Chen, X. Ma, Q.-K. Xue, and S. B. Zhang, Phys. Rev. B **87**, 220503 (2013).

[22] H.-Y. Cao, S. Tan, H. Xiang, D. L. Feng, and X.-G. Gong, Phys. Rev. B **89**, 014501 (2014).

[23] Y. Xie, H.-Y. Cao, Y. Zhou, S. Chen, H. Xiang, and X.-G. Gong, Sci. Rep. **5**, 10011 (2015).

[24] K. V. Shanavas and D. J. Singh, Phys. Rev. B **92**, 035144 (2015).

[25] F. Zheng, L.-L. Wang, Q.-K. Xue, and P. Zhang, Phys. Rev. B **93**, 075428 (2016).

[26] T. Berlijn, H.-P. Cheng, P. J. Hirschfeld, and W. Ku, Phys. Rev. B **89**, 020501 (2014).
[27] F. Zheng, Z. Wang, W. Kang, and P. Zhang, Sci. Rep. **3**, 2213 (2013).
[28] K. Liu, B.-J. Zhang, and Z.-Y. Lu, Phys. Rev. B **91**, 045107 (2015).
[29] P. D. Johnson, H.-B. Yang, J. D. Rameau, G. D. Gu, Z.-H. Pan, T. Valla, M. Weinert, and A. V. Fedorov, Phys. Rev. Lett. **114**, 167001 (2015).
[30] G. Kresse and J. Furthmüller, Comput. Mater. Sci. **6**, 15 (1996).
[31] G. Kresse and J. Furthmüller, Phys. Rev. B **54**, 11169 (1996).
[32] J. P. Perdew, K. Burke, and M. Ernzerhof, Phys. Rev. Lett. **77**, 3865 (1996).
[33] P. E. Blöchl, Phys. Rev. B **50**, 17953 (1994).
[34] G. Kresse and D. Joubert, Phys. Rev. B **59**, 1758 (1999).
[35] J. Klimeš, D. R. Bowler, and A. Michaelides, Phys. Rev. B **83**, 195131 (2011), the optPBE-vdW method is used in the present calculations.
[36] Y. Qi, S. H. Rhim, G. F. Sun, M. Weinert, and L. Li, Phys. Rev. Lett. **105**, 085502 (2010).
[37] E. T. Goodwin, Proc. Cambridge Philos. Soc. **35**, 205 (1939); **35**, 221 (1939); **35**, 232 (1939).
[38] J. W. Davenport, R. E. Watson, and M. Weinert, Phys. Rev. B **37**, 9985 (1988).
[39] M. X. Chen and M. Weinert, Nano Lett. **14**, 5189 (2014).
[40] S. V. Borisenko, D. V. Evtushinsky, Z.-H. Liu, I. Morozov, R. Kappenberger, S. Wurmehl, B. Buchner, A. N. Yaresko, T. K. Kim, M. Hoesch, T. Wolf, and N. D. Zhigadlo, Nat. Phys. **12**, 311 (2016).